Pulsed γ-ray properties of Crab pulsar in a retarded dipole with a current-induced magnetic field

Shan Chang, Li Zhang and Xiang Li

Department of Astronomy, School of Physical Science and Technology, Key Laboratory of Astroparticle Physics of Yunnan Province, Yunnan University, Kunming 650091, China; *lizhang@ynu.edu.cn*

Abstract Motivated by the *Fermi* observations of some γ-ray pulsars in which the phases of radio and γ-ray peaks are almost the same, we investigate the outer gap model in a retarded dipole with a current-induced magnetic field and apply it to explain pulsed γ-ray properties of the Crab pulsar. Our results show that the observed γ-ray energy-dependent light curves, which almost align with the radio light curve and phase averaged spectrum for the Crab pulsar, are reproduced well.

Key words: gamma rays: theory — pulsars: general — pulsars: individual (Crab) — stars: neutron

1 INTRODUCTION

Some γ-ray pulsars have been detected that have the following feature: the phases of radio and γ-ray peaks are almost the same (Abdo et al. 2013). Such an observed property should be included when modeling the gamma-ray emission from pulsars.

Charged particles (electrons and positrons) are generally believed to be accelerated to relativistic energy in some regions of a pulsar magnetosphere (these regions are often called gaps), and they will generate pulsed photon radiation from radio to γ-ray bands. Therefore, the structure of a three dimensional (3D) magnetosphere becomes a key factor for constructing 3D emission models. Currently available approximations of the pulsar magnetosphere mainly include a vacuum retarded magnetic dipole (Deutsch 1955) and a force-free (FF) magnetosphere (e.g., Spitkovsky 2008; Bai & Spitkovsky 2010b). For example, in the first approximation, 3D outer gap (OG) models (e.g. Cheng et al. 2000; Zhang & Cheng 2001, 2002), two-pole caustic models (e.g., Dyks & Rudak 2003), and slot gap models (e.g., Harding et al. 2008) have been established. Moreover, an annular gap model has been constructed in the approximation of an FF magnetosphere (Bai & Spitkovsky 2010a). However, current studies show that a real pulsar magnetosphere has electric currents along the magnetic field and so could be between the above approximations of the pulsar magnetosphere. The existence of electric currents will create a perturbed magnetic field relative to the dipole field and results in a distortion of the magnetic field. In the frame of a static magnetic dipole, Muslimov & Harding (2009) obtained an analytic solution of the magnetic field well within the light cylinder (LC), including two parts of the magnetic field: a pure static dipole magnetic field and a magnetic field created by electric currents in the open areas of the innermost magnetosphere. Such a solution has been simply extended to the retarded dipole (Romani & Watters 2010). Furthermore, Li & Zhang

(2011) derived an analytical solution in the approximation of the retarded magnetic dipole, which also includes two parts consisting of a pure retarded dipole magnetic field and a current-induced perturbed magnetic field.

In this paper, using the analytic approximation by Li & Zhang (2011), we will construct a 3D model explaining energy-dependent light curves and phase-averaged spectra for pulsars in which the phases of both radio and γ-ray peaks are essentially the same, and apply it to the Crab pulsar.

In Section 2, we briefly review the 3D OG model including the magnetic field and the emission geometry in the magnetosphere. In Section 3, we give the results of the modeling light curves and phase-averaged energy spectra. In the final Section, we summarize our results and discuss.

2 3D OUTER GAPS

As mentioned in Cheng et al. (2000), to construct a 3D OG model, we need to know the structure of a 3D pulsar magnetosphere. In this paper, we will use the analytic results given by Li & Zhang (2011) and now briefly introduce them as follows. The local value of a retarded magnetic field is approximated as (Li & Zhang 2011)

$$B'^r = B^r + \epsilon B^r_{\mathrm{p}}, \tag{1}$$

where ϵ is the perturbation amplitude describing the strength of the perturbed magnetic field, B^r_{p}, relative to the retarded magnetic field strength, B^r. The expressions describing these magnetic field strengths are

$$B^r = \widehat{r}\left[\widehat{r}\cdot\left(\frac{3m^r}{r^3} + \frac{3\dot{m}^r}{cr^2} + \frac{\ddot{m}^r}{c^2r}\right)\right] - \left(\frac{m^r}{r^3} + \frac{\dot{m}^r}{cr^2} + \frac{\ddot{m}^r}{c^2r}\right), \tag{2}$$

and

$$B^r_{\mathrm{p}} = \widehat{r}\left[\widehat{r}\cdot\left(\frac{3m^r_{\mathrm{p}}}{r^3} + \frac{3\dot{m}^r_{\mathrm{p}}}{r^3} + \frac{\ddot{m}^r_{\mathrm{p}}}{c^2r}\right)\right] - \left(\frac{m^r_{\mathrm{p}}}{r^3} + \frac{\dot{m}^r_{\mathrm{p}}}{cr^2} + \frac{\ddot{m}^r_{\mathrm{p}}}{c^2r}\right), \tag{3}$$

where m^r is the magnetic moment of B^r. Similarly, $m'^r = m^r + \epsilon m^r_{\mathrm{p}}$, where m'^r is the magnetic moment of B'^r. For details of such a magnetic field see Li & Zhang (2011). Then we can simulate the 3D structure of the pulsar magnetosphere using the results given by Li & Zhang (2011), where the last closed field lines can be calculated by using

$$(x_0, y_0, z_0) = \left[a_0 R_{\mathrm{p}}\cos(\phi_{\mathrm{p}}), a_0 R_{\mathrm{p}}\sin(\phi_{\mathrm{p}}), (R_0^2 - a_0^2 R_{\mathrm{p}}^2)^{\frac{1}{2}}\right],$$

where $R_{\mathrm{p}} = R_0(R_0/R_L)^{\frac{1}{2}}$, $R_L = c\Omega^{-1}$, Ω is the angular velocity of the pulsar, ϕ_{p} is the azimuthal angle about the magnetic axis, and a_0 is a scaling factor corresponding to the footpoints of the last closed field lines.

2.1 OG Geometry

OGs exist in this 3D pulsar magnetosphere, and the OG geometry in the (Ω, m) plane is described as follows:

(1) *Inner and Outer boundaries*. An OG lies at the region from the inner boundary to the LC in the open field line region. At the inner boundary, the ratio of the z-component of the magnetic field strength, B_z, to the magnetic field strength, B, satisfies

$$B_z/B = [2\pi/\Omega B]j_g(\phi_{\mathrm{p}})j_g(0)\left[r_{\mathrm{null}}(0)/r_{\mathrm{null}}(\phi_{\mathrm{p}})\right],$$

where $j_g(0)$ is the current density carried by the pairs produced in the OG at the radial distance $r_{\mathrm{null}}(0)$ with polar cap angle $\phi_{\mathrm{p}} = 0$ on the last closed field lines (Tang et al. 2008).

(2) *A vertical thickness* $H(r, \alpha, \phi_{\rm p})$. Following Zhang et al. (2004), a dimensionless quantity (called a fractional size)

$$f(r, \alpha, \phi_{\rm p}) = H(r, \alpha, \phi_{\rm p})/R_L$$

is used to describe the vertical thickness of the OG, which varies as a function of the inclination angle α, $\phi_{\rm p}$ and the radial distance r from a pulsar with a rotation period P and a surface magnetic field strength

$$B_* = 10^{12} \times B_{12} \ {\rm G} \,.$$

When

$$r \geq r_{\rm null}(\phi_{\rm p}) \,, \quad f(r, \alpha, \phi_{\rm p}) = \chi(r, \alpha, P, B_*) f_0(P, B_*)$$

with

$$f_0(P, B_*) \approx 5.5 P^{\frac{26}{21}} B_{12}^{-4/7}$$

(see Zhang & Cheng 1997) and

$$f(r, \alpha, \phi_{\rm p}) = (r_{\rm null}, \alpha, \phi_{\rm p}) \big[B_{\rm null}/B(r) \big]^{\frac{1}{2}} \,,$$

when $r < r_{\rm null}(\phi_{\rm p})$ (Zhang & Li 2009), where $\chi(r, \alpha, P, B)$ is the revised factor in which the effects of the inclination angle and magnetic field geometry are included (Zhang & Jiang 2006).
(3) The azimuthal extension $\Delta\phi_p$. Following Tang et al. (2008), the value of $\Delta\phi_p$ is estimated by the local pair production condition.

In such a 3D OG geometry, the locally accelerating electric field can be expressed as follows (Tang et al. 2008):

$$E_\parallel = \Omega B H^2 / c s(r) \quad {\rm for} \quad r \geq r_{\rm null(\phi_{\rm p})}$$

and

$$E_\parallel = E_\parallel (r_{\rm null}(\phi_p)) \big[(r/r_{\rm in})^2 - 1 \big] / \big[(r_{\rm null}(\phi_p)/r_{\rm in})^2 - 1 \big] \quad {\rm for} \quad r < r_{\rm null}(\phi_p),$$

where $s(r)$ is the radius of curvature and $r_{\rm in}$ is the radial distance of the inner boundary. Note that $r_{\rm null}$ is a function of ϕ_p (see the right panel of Fig. 1), so $E_\parallel$ is different for various values of ϕ_p.

We now consider the emission patterns in the 3D OG geometry mentioned above. The direction, $\boldsymbol{n}$, of the particle motion is assumed to be the emission direction of the photons and can be calculated in the inertial observer's frame (see eq. (6) of Takata et al. 2007). This emission direction is usually expressed by using the viewing angle ζ and rotation phase Φ (i.e., the so-called (ζ, Φ) plane). Therefore, for the emission direction with an azimuthal angle Φ_n and a parallel component $n_\parallel$ of $\boldsymbol{n}$ at location $\boldsymbol{r}$, the viewing angle and the rotation phase can be calculated by using $\cos\zeta = n_\parallel$ and $\Phi = -\Phi_n - \boldsymbol{r} \cdot \boldsymbol{n}/\boldsymbol{R}_L$, respectively.

The photon emission pattern on the (ζ, Φ) plane for the Crab pulsar with $P = 33.6$ ms and $B_* = 3.8 \times 10^{12}$ G is shown in the left panel of Figure 1, where the emission (black lines) is from the south pole with (ζ, Φ) and that (gray lines) from the north pole with $(\zeta - 180°, \Phi + 180°)$.

If the viewing angle ζ is given, a light curve can be estimated from the emission pattern by simply assuming uniform γ-ray emissivity. To see how different parts of the light curve depend on the radial distance for different values of azimuthal angle ϕ_p, we divide the light curve into three parts: the first peak P1, the bridge, and the second peak P2, and show the variation of r/R_L with ϕ_p in the right panel of Figure 1, where the emission pattern corresponds to the left panel of Figure 1 and $\zeta = 60°$ is assumed. For comparison, the change of $r_{\rm null}$ with ϕ_p is also shown. Note that some phase values only correspond to each $\phi_{\rm p}$ value. From the right panel of this figure, P1 comes from the incoming emission from emitting positions that have $r/R_{\rm L} \sim 0.15$ to 0.85, which are below the null charge surface, for $\Delta\phi_p \approx 210°$ in the north pole; both bridge and P2 come from the outgoing emissions in the south pole.
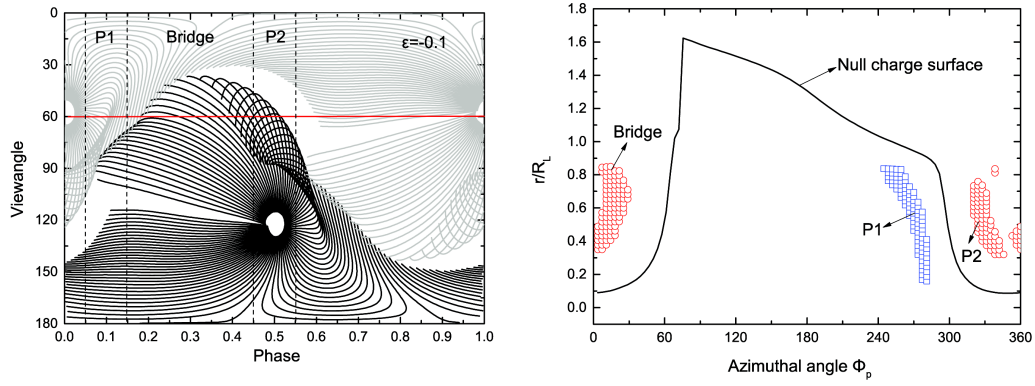
Fig. 1 *Left panel*: Photon emission pattern on the (ζ, Φ) plane for the Crab pulsar with $P = 33.6$ ms and $B_* = 3.8 \times 10^{12}$ G. The model parameters are $\alpha = 55°$, $\epsilon = -0.1$, $a_1 = 0.98$ and $f_0 = 0.55$. The black and gray lines represent emissions from the south and the north poles, respectively. *Right panel*: The variation of radial distance r/R_L with the azimuthal angle ϕ_p for the three parts (P1, bridge and P2) of the light curve, where the emission pattern corresponds to the left panel and $\zeta = 60°$. Blue squares and red circles represent emitting positions from the north and south poles in the $(r/R_L, \phi_p)$ plane, respectively. For comparison, the change of $r_{\rm null}$ with ϕ_p is also shown (solid curve).

3 MODELING LIGHT CURVES AND PHASE-AVERAGED ENERGY SPECTRA

In the calculation of the energy-dependent light curves and the non-thermal radiation spectra, we need to know the radiation mechanisms. Here, we briefly describe the physical processes for γ-ray emission from the Crab pulsar in the OG model (for details see Tang et al. 2008; Zhang & Li 2009). In the OGs, electron and positron $(e^{\pm})$ pairs are accelerated to relativistic energy by the parallel electric field $E_\parallel$ which varies with α, ϕ_p and r (see Eq. (4)), and then primary curvature photons with typical energies of $E_{\rm cur}$ are produced through curvature radiation of the accelerated $e^{\pm}$ pairs. These primary curvature photons can be divided into two types: escaping (or surviving) curvature photons and colliding curvature photons. The former will escape from the magnetosphere of the Crab pulsar due to a longer mean free path with respect to the LC radius, resulting in the energy spectrum $dN_{\rm cur,sur}/dE_\gamma dt$ which peaks at ~ 10 GeV, with

$$F_{\rm cur,sur} = F_{\rm cur}e^{-\tau(E_\gamma, r)} ,$$

where the attenuation depth is

$$\tau(E_\gamma, r) = l(r) \int_{\epsilon_{\min}}^{\epsilon_{\max}} \left[n_{\rm syn}(\epsilon, r) + n_X(\epsilon, r) \right] \sigma_{\gamma\gamma}(E_\gamma, \epsilon) d\epsilon$$

(Tang et al. 2008). The latter will interact with soft photons produced by the synchrotron radiation of secondary $e^{\pm}$ pairs through the photon-photon $e^{\pm}$ production process, which leads to even more secondary $e^{\pm}$ pairs, where the absorption of the primary curvature photons in the magnetospheric soft photon field is calculated by using the method given by Tang et al. (2008) and the typical collision angle is about 0.45 rad. These secondary $e^{\pm}$ pairs with their pitch angles $\varphi(r)$, which are given by $\sin\varphi(r) = \eta(r, \alpha)(r/R_L)^{1/2}\sin\varphi(R_L)$, will emit non-thermal photons through synchrotron radiation with energy spectrum $dN_{\rm syn}/dE_\gamma dt$ and inverse Compton scattering (ICS) with energy spectrum $dN_{\rm ICS}/dE_\gamma dt$. There are two kinds of soft photon fields: synchrotron photons with a number density of

$$n_{\rm syn}(\epsilon, r) = F_{\rm syn}(\epsilon, r)/(cr^2\pi\varphi^2(r))$$

which are produced by secondary $e^\pm$ through synchrotron radiation and thermal photons from the stellar surface with a number density of

$$n_X(\epsilon, r) = \left[1/\pi^2(\hbar c)^3\right]\left[\epsilon^2/\exp(\epsilon/kT) - 1\right](R/r)^2 \,.$$

Here, the soft photon density is assumed to have an isotropic distribution (Blumenthal & Gould 1970; Tang et al. 2008). Therefore, the total photon flux of the Crab pulsar received on the Earth is (Zhang & Li 2009)

$$F(E_\gamma) = \sum_i F_i(E_\gamma, r)\,, \tag{4}$$

where

$$F_i = [1/D^2]\sum_r \left[dN_i(E_\gamma, r)/dE_\gamma dt\right]/\Delta\Omega; \quad i = \mathrm{syn},\ \mathrm{ICS},\ \mathrm{cur},\ \mathrm{sur};$$

$D = 2$ kpc is the distance to the Crab pulsar; $\Delta\Omega = 4\pi f_\Omega$ is the solid angle of gamma-ray radiation; and f_Ω is the flux correction factor which is related to α, $f(r, \alpha, \phi_\mathrm{p})$ and ζ (see eq. (9) in Li & Zhang 2010).

Next we consider the light curves in different energy bands. Based on the energy spectra, we can calculate the number of photons in an energy range from E_1 to E_2 by the integral given in (Li & Zhang 2010)

$$N_\mathrm{ph}(E_1 \leq E_\gamma \leq E_2) \propto \int_{E_1}^{E_2} \sum_i \frac{dN_i}{dE_\gamma dt} dE_\gamma\,. \tag{5}$$

Figure 2 shows the calculated and observed γ-ray energy-dependent light curves with energy greater than 100 MeV for the Crab pulsar. The observed data appear to be phase-aligned between radio at 1.4 GHz (blue line) and γ-ray (red histogram) pulse profiles, where $\delta = 0.11 \pm 0.01$ is the offset of the mode of the leading peak from the zero phase (or the fiducial phase) (see the description of Abdo et al. 2013), and $\Delta = 0.41 \pm 0.01$ is the separation between two gamma-ray peaks for the Crab pulsar (Abdo et al. 2013). In our model, $\Delta = 0.40$ is approximately equal to the observed value (see Fig. 2). From the figure, our result can reproduce the observed light curve well.

In Figure 3, we show the predicted and observed energy-dependent light curves at 100 MeV – 300 MeV, 300 MeV – 1 GeV and 1 GeV – 3 GeV bands for the Crab pulsar. We need to point out that the flux of the first peak (P1) totally comes from the incoming emission below the null surface from the north pole. By comparing Figure 1 with Figure 3, we find the green and blue solid curves in Figure 3 correspond to the black and grey solid curves in Figure 1, which come from the emissions radiated by the south and north poles, respectively. It can be seen that our results are consistent with the observed data, moreover the contributions of the two poles to the light curves are different.

In Figure 4, we show a comparison between simulated and observed phase-averaged spectra from the γ-ray band for the Crab pulsar. Dot-dashed lines represent the spectra of ICS from secondary pairs and dashed curves represent the spectra of the surviving curvature, the black dot-dashed and dashed curves are the spectra produced at the north pole, and the gray dot-dashed and dashed curves are the spectra produced at the south pole. The black solid curve represents the total spectrum. The blue (green) curve represents the sum of the ICS spectrum and the surviving curvature spectrum in the north (south) pole. Although the emission from the south pole is stronger than that from the north pole, the emission from the north pole is concentrated in the narrow phase region (i.e. P1 region), so P1 is higher than P2. As Figure 4 shows, there are two sources that contribute to the total non-thermal photons produced in the GeV band for the Crab pulsar. One is the photons produced by ICS from secondary pairs and the other is the surviving curvature photons.
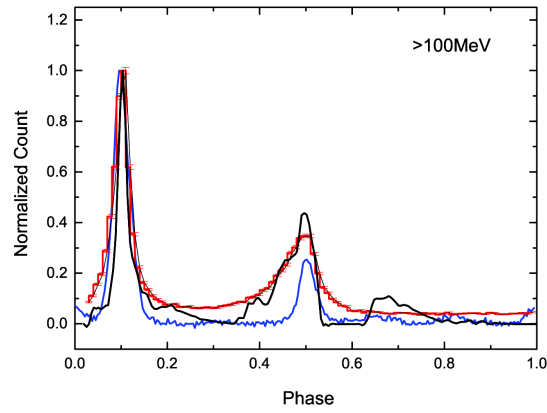
Fig. 2 γ-ray energy-dependent light curves with energy greater than 100 MeV for the Crab pulsar. The black solid curve is the theoretical prediction in this OG model. The blue line is the observed radio result with 1.4 GHz and the red histogram is the observed γ-ray result (Abdo et al. 2013). In the calculation, $\alpha = 55°$, $\epsilon = -0.1$, $\zeta = 60°$, $a_1 = 0.98$ and $f(R_L) \approx 0.16$ are used.
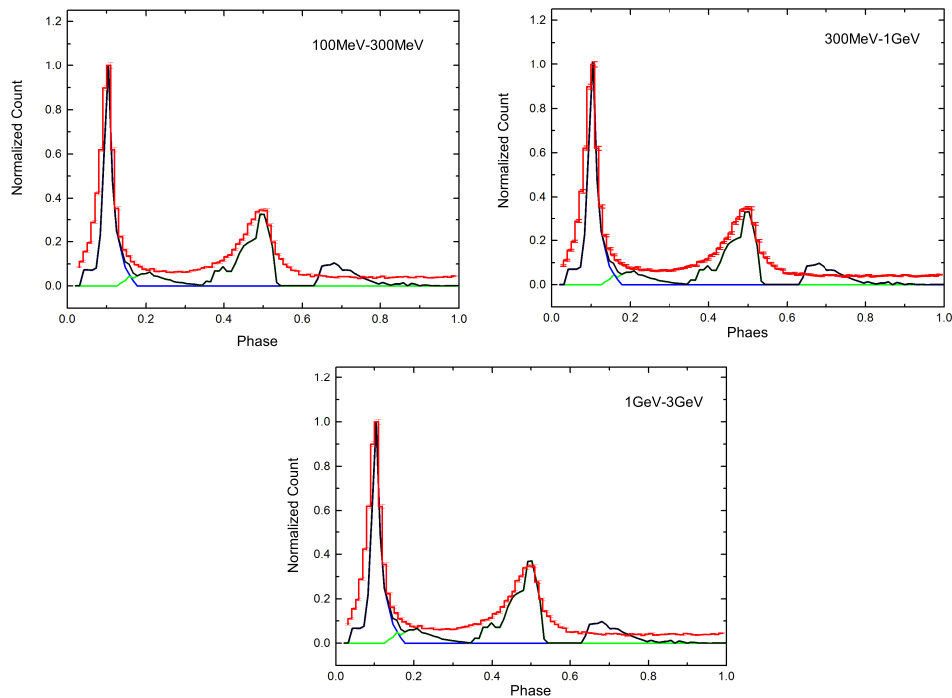
Fig. 3 Energy-dependent light curves at 100 MeV–300 MeV, 300 MeV–1 GeV and 1 GeV–3 GeV for the Crab pulsar. The black solid curve at each energy band represents the predicted light curve which is the sum of the light curves from the south pole (*green solid curve*) and the north pole (*blue solid curve*). The red histograms represent observed data (Abdo et al. 2013). In the calculation, $\alpha = 55°$, $\epsilon = -0.1$, $\zeta = 60°$, $a_1 = 0.98$ and $f(R_L) \approx 0.16$ are used.
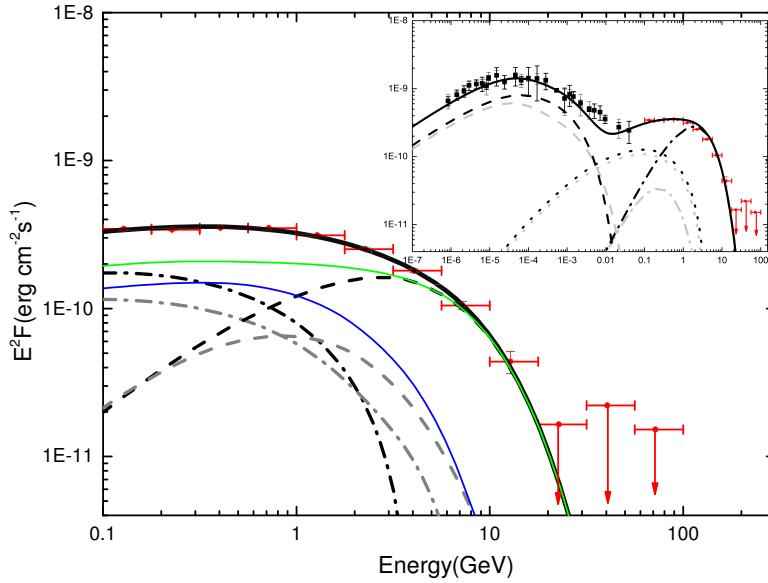
Fig. 4 Phase-averaged γ-ray spectra predicted in this OG model and observed data with energy greater than 100 MeV for the Crab pulsar. The inset shows the phase-averaged γ-ray spectra with energy from 10^{-7} to 10^2 GeV. The black solid curve represents the total spectrum. The black (grey) dot-dashed curve is the ICS spectrum of secondary $e^{\pm}$ pairs in the north (south) pole, and black (grey) dashed curves represent the spectrum of the surviving curvature photons in the north (south) pole. The blue (green) curve represents the sum of the ICS spectrum and the surviving curvature spectrum in the north (south) pole. The solid boxes represent the observed data from Kuiper et al. (2001). The red data points represent the observed data from *Fermi* LAT (Abdo et al. 2013). In the calculation, $\alpha = 55°$, $\epsilon = -0.1$, $\zeta = 60°$, $a_1 = 0.98$ and $f(R_L) \approx 0.16$ are used.

4 SUMMARY AND DISCUSSION

In this paper, pulsed γ-ray properties of the Crab pulsar have been investigated in the modified version of the retarded magnetic dipole. In the structure of such a pulsar magnetosphere in which electric currents induce a perturbation in the magnetic field, observed γ-ray energy-dependent light curves, which almost align with the radio light curve (see Fig. 2) and phase averaged spectrum (see Fig. 4) for the Crab pulsar, are reproduced well in the OG model used here. The model parameters are $\alpha = 55°$, $\epsilon = -0.1$, $\zeta = 60°$, $a_1 = 0.98$, $f(R_L) \approx 0.16$ and $\epsilon = -0.1$. Note that in the vacuum-retarded dipole approximation of the pulsar magnetosphere, Li & Zhang (2010) calculated the energy-dependent light curves and spectra for the Crab pulsar in the OG model given by Tang et al. (2008) (for the revised version see Zhang & Li 2009), but they did not consider the case in which the phases of radio and γ-ray peaks are almost the same.

Since the pulsar magnetosphere plays an important role in the calculation of light curves and spectra, various approximations of a real pulsar magnetosphere have been investigated. For example, Romani & Watters (2010) pointed out that the retarded dipole field with a current-induced perturbed field can act as a good approximation of the FF magnetic field, and Li & Zhang (2011) obtained the analytic solution of such a field, where $\epsilon > 0$ and $\epsilon < 0$ should have opposite roles and the main reason causing the phenomenon of phase alignment is the different values of ϵ. On the other hand, 3D pulsar magnetosphere models that incorporate finite conductivity are more realistic. Dissipative pul-

sar magnetospheres have been established (Kalapotharakos et al. 2012; Li et al. 2012) and have been applied to study the shapes of gamma-ray light curves of pulsars (Kharb et al. 2012; Kalapotharakos et al. 2014).

References

Abdo, A. A., Ajello, M., Allafort, A., et al. 2013, ApJS, 208, 17
Bai, X.-N., & Spitkovsky, A. 2010a, ApJ, 715, 1282
Bai, X.-N., & Spitkovsky, A. 2010b, ApJ, 715, 1270
Blumenthal, G. R., & Gould, R. J. 1970, Reviews of Modern Physics, 42, 237
Cheng, K. S., Ruderman, M., & Zhang, L. 2000, ApJ, 537, 964
Deutsch, A. J. 1955, Annales d'Astrophysique, 18, 1
Dyks, J., & Rudak, B. 2003, ApJ, 598, 1201
Harding, A. K., Stern, J. V., Dyks, J., & Frackowiak, M. 2008, ApJ, 680, 1378
Kalapotharakos, C., Kazanas, D., Harding, A., & Contopoulos, I. 2012, ApJ, 749, 2
Kalapotharakos, C., Harding, A. K., & Kazanas, D. 2014, ApJ, 793, 97
Kharb, P., O'Dea, C. P., Tilak, A., et al. 2012, ApJ, 754, 1
Kuiper, L., Hermsen, W., Cusumano, G., et al. 2001, A&A, 378, 918
Li, J., Spitkovsky, A., & Tchekhovskoy, A. 2012, ApJ, 746, 60
Li, X., & Zhang, L. 2010, ApJ, 725, 2225
Li, X., & Zhang, L. 2011, ApJ, 743, 113
Muslimov, A. G., & Harding, A. K. 2009, ApJ, 692, 140
Romani, R. W., & Watters, K. P. 2010, ApJ, 714, 810
Spitkovsky, A. 2008, ApJ, 682, L5
Takata, J., Chang, H.-K., & Cheng, K. S. 2007, ApJ, 656, 1044
Tang, A. P. S., Takata, J., Jia, J. J., & Cheng, K. S. 2008, ApJ, 676, 562
Zhang, L., & Cheng, K. S. 1997, ApJ, 487, 370
Zhang, L., & Cheng, K. S. 2001, MNRAS, 320, 477
Zhang, L., & Cheng, K. S. 2002, ApJ, 569, 872
Zhang, L., Cheng, K. S., Jiang, Z. J., & Leung, P. 2004, ApJ, 604, 317
Zhang, L., & Jiang, Z. J. 2006, A&A, 454, 537
Zhang, L., & Li, X. 2009, ApJ, 707, L169